CrossMark
click for updates

Measurement of the Na$_2$ $5^1\Sigma_g^+ \rightarrow A^1\Sigma_u^+$ and $6^1\Sigma_g^+ \rightarrow A^1\Sigma_u^+$ transition dipole moments using optical-optical double resonance and Autler–Townes spectroscopy

Aydin Sanli,[1] Xinhua Pan,[1] Sylvie Magnier,[2] John Huennekens,[3] A. Marjatta Lyyra,[1] and Ergin H. Ahmed[1,a)]

[1]*Physics Department, Temple University, Philadelphia, Pennsylvania 19122, USA*
[2]*Université Lille, CNRS, UMR8523-PhLAM-Laboratoire de Physique des Lasers, Atomes et Molecules, F-59000 Lille, France*
[3]*Department of Physics, Lehigh University, 16 Memorial Drive East, Bethlehem, Pennsylvania 18015, USA*

Accurate knowledge of transition dipole moment matrix elements is crucial since important parameters associated with the interaction of light with matter, such as emission and absorption line intensities, lifetimes, and Einstein coefficients, depend on these matrix elements. We report here an experimental study of the Na$_2$ $5^1\Sigma_g^+ \leftrightarrow A^1\Sigma_u^+$ and $6^1\Sigma_g^+ \leftrightarrow A^1\Sigma_u^+$ electronic transition dipole moments and their dependence on internuclear distance. We have measured absolute transition dipole matrix elements for ro-vibrational transitions of the Na$_2$ $5^1\Sigma_g^+ \leftrightarrow A^1\Sigma_u^+$ and $6^1\Sigma_g^+ \leftrightarrow A^1\Sigma_u^+$ electronic transitions using Autler-Townes and optical-optical double resonance spectroscopy, and we compare the results to *ab initio* theoretical values [A. Sanli *et al., J. Chem. Phys.* **143**, 104304 (2015)]. *Published by AIP Publishing.* https://doi.org/10.1063/1.5002726

I. INTRODUCTION

Interactions between the Na$^+$ + Na$^-$ ion-pair Coulomb potential and the $5^1\Sigma_g^+$ and $6^1\Sigma_g^+$ electronic states of Na$_2$ cause these states to exhibit double wells and shoulders.[1–5] Because of the shallow, open nature of these states, the ro-vibrational wavefunctions for the $5^1\Sigma_g^+$ and $6^1\Sigma_g^+$ electronic states acquire unusually large amplitudes in the large internuclear distance, R, region of the potential energy functions. Because the electronic configuration of the adiabatic potentials changes rapidly in the interaction region, the electronic transition dipole matrix elements of the $5^1\Sigma_g^+ \leftrightarrow A^1\Sigma_u^+$ and $6^1\Sigma_g^+ \leftrightarrow A^1\Sigma_u^+$ transitions also exhibit rapidly changing behavior.[4,6]

Traditionally, transition dipole matrix elements have been determined experimentally using spectral line intensities or lifetimes.[7] However, usually only *relative* transition dipole moments can be determined with these methods. For example, fluorescence intensity measurements do not give absolute dipole matrix elements because absolute intensities are difficult to determine, the emission is generally not isotropic, and the wavelength and polarization dependence of the detection system must be taken into account. However, since the intensities of emission (fluorescence) lines are proportional to the square of the transition dipole matrix element and the 4th power of the transition frequency ($I_{fluor} \propto \nu^4 |\mu|^2$), ratios of line intensities divided by ν^4 yield ratios of dipole matrix elements squared.

Autler-Townes (AT) spectroscopy is an alternative method that provides absolute transition dipole matrix elements (from AT splittings of spectral lines) for sufficiently strong transitions.[8–11] Such measurements can be used to put relative dipole matrix elements, obtained, for example, from fluorescence measurements, on an absolute scale.[8]

We present here an experimental study of the transition dipole moment functions of the $5^1\Sigma_g^+ \leftrightarrow A^1\Sigma_u^+$ and $6^1\Sigma_g^+ \leftrightarrow A^1\Sigma_u^+$ electronic transitions of Na$_2$. The matrix elements of specific ro-vibrational transitions were obtained experimentally using a combination of resolved fluorescence line intensities and AT splittings. From each full set of measured matrix elements, the electronic component of the transition dipole moment function, $\mu_e(R)$, and its dependence on internuclear distance were extracted. This work is a follow-up of the previously published lifetime calculations[6] from our group, in which electronic transition dipole moment functions, $\mu_e(R)$, obtained from *ab initio* calculations, were used to calculate the lifetimes of the ro-vibrational levels of the $3^1\Sigma_g^+$, $4^1\Sigma_g^+$, $5^1\Sigma_g^+$, and $6^1\Sigma_g^+$ electronic states of Na$_2$.

II. EXPERIMENT

The experimental setup for Autler-Townes spectroscopy and resolved fluorescence experiments is depicted in Fig. 1. Sodium vapor was generated in a five-arm heat pipe oven.[12] Argon with a pressure of about 300-400 mTorr was used as a buffer gas to keep the sodium vapor away from the windows. The operating temperature of the heat pipe oven was 600-800 K.

In both experiments, a pair of single-mode, frequency-stabilized, tunable, continuous-wave (cw) ring dye lasers (Coherent, Inc., Autoscan 699-29) were pumped by 6 W of 532 nm light from two frequency-doubled Nd:YVO$_4$ lasers

---

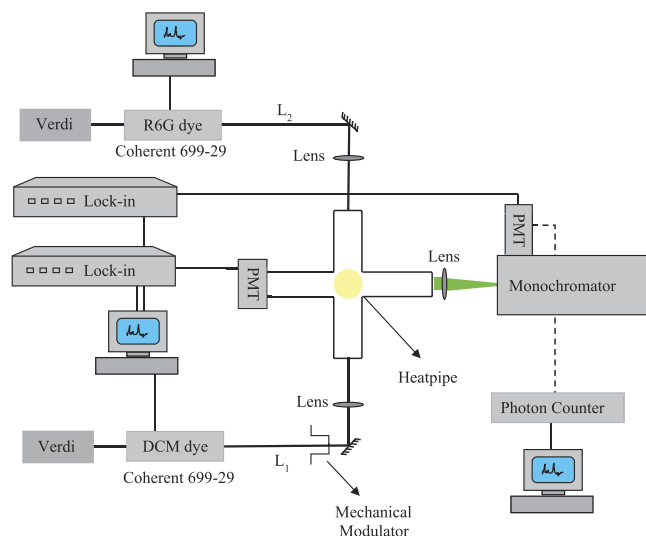a)Author to whom correspondence should be addressed: erahmed@temple.edu

FIG. 1. Experimental schematic of Autler-Townes spectroscopy and resolved fluorescence experiments. L_1 and L_2 are the tunable pump/probe and the coupling lasers, respectively. The tunable ring dye lasers are pumped by Verdi V10 lasers. The total fluorescence collection PMT (shown here on the left side-arm) was actually mounted on the top arm of the heat pipe. A BOMEM FT-IR spectrometer was used to calibrate the frequencies of the probe and coupling lasers.

(Coherent, Inc., Verdi V10). The pump/probe laser (L_1) was operated with DCM dye, while the coupling laser (L_2) used R6G dye.

Resolved florescence spectra were acquired using a SPEX 1404 double monochromator, which was scanned while the pump/probe and coupling lasers were each fixed to the appropriate resonance frequency. A photon counter was used to process the signal from the photomultiplier tube (PMT) placed at the monochromator exit slit. Line intensities in the recorded spectra were corrected for the wavelength variation of the monochromator and PMT response using a white light, tungsten-halogen lamp.[13] A second photomultiplier tube (Hamamatsu R928), with bandpass filters, mounted on the top window of the heat pipe, was used to monitor total $5^1\Sigma_g^+ \rightarrow A^1\Sigma_u^+$ or $6^1\Sigma_g^+ \rightarrow A^1\Sigma_u^+$ fluorescence during the optical-optical double resonance (OODR) resolved fluorescence scans. This was used to ensure that both lasers remained on resonance while the resolved fluorescence was recorded.

In the AT splitting measurements, the coupling laser (L_2) was kept on resonance while the pump/probe laser (L_1) was scanned. In order to minimize the residual Doppler linewidth, the two lasers counter-propagated through the vapor. Once the AT splitting was observed, alignment of the beams was optimized to maximize the splitting.

To ensure that the electric field amplitude, E, of the coupling laser was homogenous over the volume probed in the AT splitting measurements, the coupling laser beam diameter was chosen to be approximately twice as large as that of the pump/probe laser. The spot sizes for L_1 and L_2 for the $5^1\Sigma_g^+ \leftarrow A^1\Sigma_u^+$ measurements were 150 μm and 260 μm, respectively, while for the $6^1\Sigma_g^+ \leftarrow A^1\Sigma_u^+$ measurements, they were 160 μm and 280 μm, respectively. The electric field amplitudes were calculated from the laser power, P, and the measured spot size, w, defined at the $1/e^2$ intensity points of the Gaussian

beam profile, using the expression $E = \sqrt{\frac{4P}{\pi c \varepsilon_0 w^2}}$. Spot sizes were determined experimentally using the razor blade technique,[14] where a razor blade is moved perpendicularly across the laser beam. The position of the razor blade is recorded at the points where 25% (d_{25}) and 75% (d_{75}) of the total power is transmitted. The spot size, w, is then calculated from the equation $w = \frac{1}{B\sqrt{2}}(d_{75} - d_{25})$ where $\operatorname{erf}(B) = \frac{1}{2}$ ($B \approx 0.47$). For each laser, the inferred power at the center of the oven includes the loss at the entrance window of the heat pipe, which was estimated to be approximately 10%, obtained from the measured total laser transmission of the cold heat pipe (through both windows).

III. RESULTS AND DISCUSSION

Using the AT splitting and resolved fluorescence methods, we have determined the transition dipole matrix elements for a number of Na$_2$ ro-vibrational transitions between the $A^1\Sigma_u^+$ state and the $5^1\Sigma_g^+$ and $6^1\Sigma_g^+$ ion-pair states. Examples of typical pump/probe laser (L_1) frequency scans showing the Autler-Townes splittings of the spectral lines induced by the interaction of the molecule with the strong coupling laser L_2 are given in Fig. 2. Such data from the AT splitting measurements were analyzed using the density matrix formalism as in previous studies.[8,9,15–17] Figure 3 shows a schematic of the
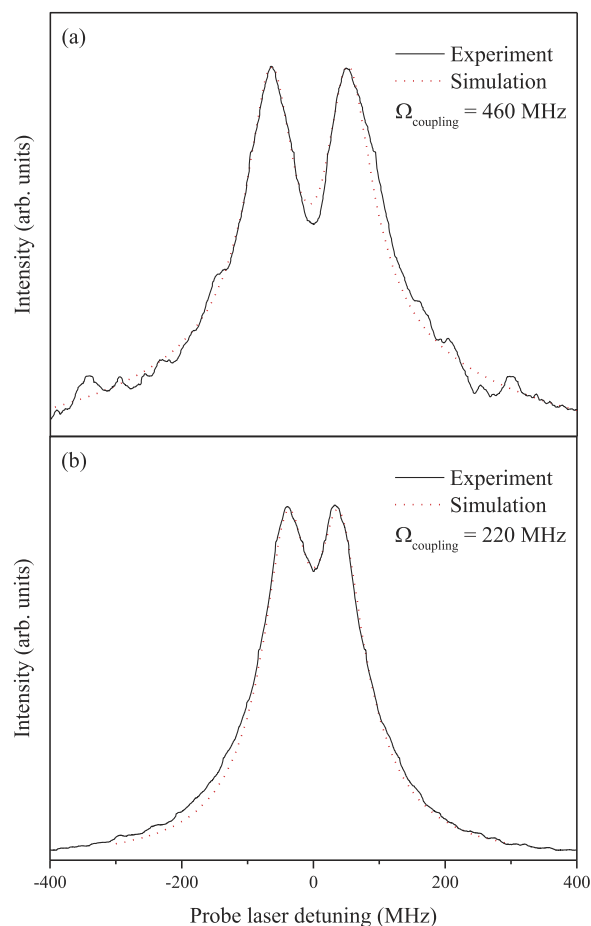

FIG. 2. The Autler-Townes splitting spectra (a) for the $5^1\Sigma_g^+(23, 21) \leftrightarrow A^1\Sigma_u^+(21, 20)$ transition and (b) for the $6^1\Sigma_g^+(15, 19) \leftrightarrow A^1\Sigma_u^+(15, 20)$ transition of Na$_2$.
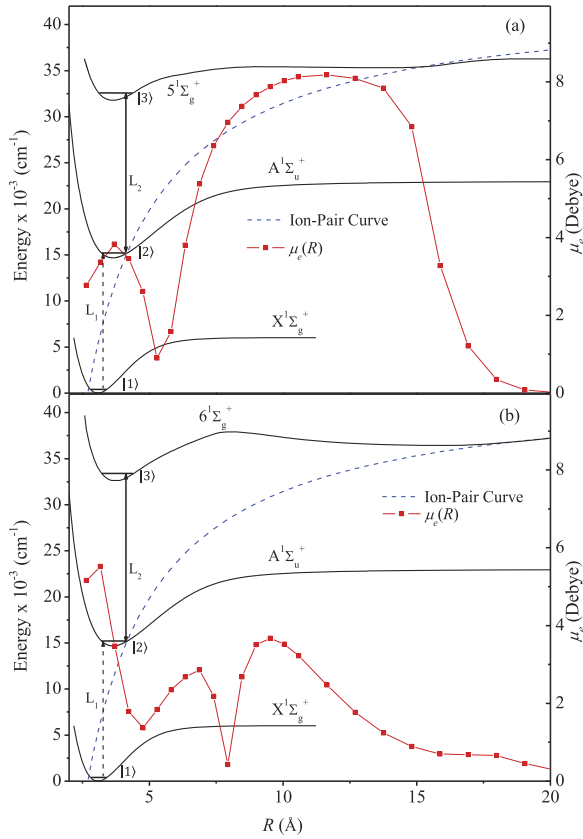
FIG. 3. The Na$_2$ OODR excitation scheme for the (a) $5^1\Sigma_g^+ \leftarrow A^1\Sigma_u^+ \leftarrow X^1\Sigma_g^+$ and (b) $6^1\Sigma_g^+ \leftarrow A^1\Sigma_u^+ \leftarrow X^1\Sigma_g^+$ transitions. L$_1$ and L$_2$ are counter-propagating pump/probe and coupling lasers, respectively. The *ab initio* transition dipole moment functions[6] are shown in red, while the blue dashed lines represent the Na$^+$ + Na$^-$ ion-pair curve.

model system, which includes three levels (labeled $|1\rangle$, $|2\rangle$, and $|3\rangle$) coupled by the two lasers (L$_1$ and L$_2$).

To simulate the AT line shape, the density matrix equations of motion,

$$\frac{\partial \rho}{\partial t} = -\frac{i}{\hbar}[H, \rho] + relaxation\ terms, \qquad (1)$$

were solved in steady state. Following Ref. 18, the Hamiltonian in the interaction picture for a three-level cascade system coupled together by the lasers L$_1$ and L$_2$ on or near resonance with the transitions $|1\rangle \leftrightarrow |2\rangle$ and $|2\rangle \leftrightarrow |3\rangle$, respectively, is given by

$$H_I = \hbar\Delta_1 |2\rangle\langle 2| + \hbar(\Delta_1 + \Delta_2)|3\rangle\langle 3| + \hbar\frac{\Omega_1}{2}(|2\rangle\langle 1| + |1\rangle\langle 2|)$$

$$+ \hbar\frac{\Omega_2}{2}(|3\rangle\langle 2| + |2\rangle\langle 3|). \qquad (2)$$
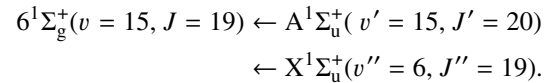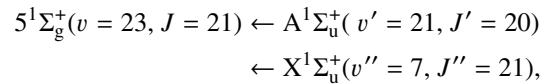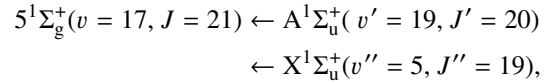
In this expression, Ω_i is the Rabi frequency, $\Omega_i \equiv \frac{\mu_{i,i+1}E_{L_i}}{\hbar}$, E_{L_i} is the electric field amplitude of the ith laser, ($i = 1, 2$), and $\mu_{i,i+1} = \langle \chi_{v_{i+1}J_{i+1}} | \mu_e(R) | \chi_{v_i J_i}\rangle$ is the transition dipole matrix element corresponding to the transition $|i + 1\rangle \leftrightarrow |i\rangle$. χ_{vJ} represents a vibrational wavefunction. To simulate our experimental spectra, we used the procedure outlined in Refs. 11, 17, and 19 for open molecular systems. In the simulation, we vary the Rabi frequency of the coupling laser to obtain the best match between the simulated and experimental line splittings. Radiative decay rates, which enter the calculation through the relaxation terms, were determined from the

ab initio calculations.[6] Rates for collisional decay of coherence (dephasing collisions), which also affect the relaxation terms, were adjusted to provide the best fit in the wings of the AT split line shape. In the simulations, we have observed that values of the radiative and dephasing rates do not significantly influence the AT spitting, which is predominantly determined by the coupling laser Rabi frequency.

From the fitted values of the coupling laser Rabi frequency, each transition dipole matrix element was calculated using the experimentally determined electric field amplitude of the coupling laser and the definition $\Omega \equiv \mu E/\hbar$.[20] In previous work, we have estimated that the uncertainty in the value of the matrix element μ obtained using this procedure to be about ±0.2 D.[10] The main contributors to the error are the ±10 μm accuracy in the spot size measurement, laser power fluctuations of 1%–2%, the absolute power calibration of the power meter used, possible deviation from collinear overlap of the laser beams, and the inherent noise in the recorded spectra.

Transition parameters and absolute experimental transition dipole matrix elements obtained from the AT splittings are listed in Table I for the Na$_2$ $5^1\Sigma_g^+ \leftrightarrow A^1\Sigma_u^+$ transitions and in Table II for the $6^1\Sigma_g^+ \leftrightarrow A^1\Sigma_u^+$ transitions studied in this work.

We have also recorded resolved fluorescence spectra from the $5^1\Sigma_g^+(v = 17, J = 21)$, $5^1\Sigma_g^+(v = 23, J = 21)$, and $6^1\Sigma_g^+(v = 15, J = 19)$ levels to the $A^1\Sigma_u^+$ state using a SPEX 1404 double grating monochromator. The excitation scheme for each case is as follows:

$$5^1\Sigma_g^+(v = 17, J = 21) \leftarrow A^1\Sigma_u^+(v' = 19, J' = 20)$$
$$\leftarrow X^1\Sigma_u^+(v'' = 5, J'' = 19),$$

$$5^1\Sigma_g^+(v = 23, J = 21) \leftarrow A^1\Sigma_u^+(v' = 21, J' = 20)$$
$$\leftarrow X^1\Sigma_u^+(v'' = 7, J'' = 21),$$

$$6^1\Sigma_g^+(v = 15, J = 19) \leftarrow A^1\Sigma_u^+(v' = 15, J' = 20)$$
$$\leftarrow X^1\Sigma_u^+(v'' = 6, J'' = 19).$$

An example of a resolved fluorescence spectrum [in this case from the $6^1\Sigma_g^+$ ($v = 15, J = 19$) level] is shown in Fig. 4.

Measured fluorescence line intensities were first corrected using the relative detection system (monochromator + PMT) efficiency versus wavelength curve obtained using the calibrated quartz-iodine lamp (1CL-200-W, 6.5A AC), which is an established secondary standard for intensity as a function of wavelength.[13] Then, using the relation $I_{fluor} \propto \nu^4|\mu|^2$, the corrected relative line intensities of the experimentally recorded resolved fluorescence spectra were used to calculate a *relative* transition dipole matrix element for each observed transition. Since at least one transition observed in each of the resolved fluorescence spectra was also studied using the Autler-Townes method, that transition could be used as a reference, and the entire set of *relative* transition dipole matrix elements from a particular resolved fluorescence scan could be scaled to yield *absolute* dipole matrix elements. (Note that, in some cases, the fluorescence reference line was the other member of a P/R doublet than that used as the AT splitting reference. This was due to the fact that fluorescence intensity

TABLE I. Transition dipole moment matrix elements (TDMM) obtained from the Autler-Townes splitting measurements and from resolved fluorescence line intensities for various $5^1\Sigma_g^+(v,J) \leftrightarrow A^1\Sigma_u^+(v',J')$ transitions.

$5^1\Sigma_g^+(v,J)$	$A^1\Sigma_u^+(v',J')$	TDMM (Debye) experiment	TDMM (Debye) theory	$\|\langle \chi_{vJ} \| \chi_{v'J'} \rangle\|$	$\overline{R}$ (Å)	$\overline{R^2}$ (Å^2)	
(4,21)	(4,20)	3.124	3.605	0.992	3.74	14.08	
(8,21)	(8,20)	3.238	3.327	0.952	3.81	14.78	
(10,21)	(10,20)	2.902	3.089	0.903	3.84	15.08	
(10,20)	(9,21)	0.767	1.005	0.264	2.73	6.41	
(11,20)	(10,21)	0.988	1.195	0.316	2.93	7.90	
(12,21)	(11,22)	1.238	1.395	0.372	3.09	9.18	
(13,21)	(13,20)	2.278	2.529	0.768	3.86	15.3	
(13,21)	(12,20)	1.389	1.646	0.444	3.26	10.45	
(13,19)	(14,18)	0.839	1.062	0.347	5.27	26.09	Autler-Townes
(15,21)	(14,20)	1.931	2.034	0.616	3.81	15.07	
(15,21)	(16,22)	0.987	1.110	0.380	5.22	25.79	
(17,21)	(16,20)	2.208	2.327	0.661	3.65	13.56	
(17,21)	(18,20)	0.894	1.051	0.374	5.15	25.34	
(20,21)	(19,20)	2.068	2.178	0.662	3.80	14.87	
(23,21)	(21,20)	1.913	2.034	0.593	3.70	14.00	
(27,21)	(24,20)	1.504	1.710	0.525	3.76	14.64	
(23,21)	(20,20)	0.561	0.667	0.180	2.46	4.55	
(23,21)	(20,22)	0.512	0.608	0.164	2.33	3.51	
(23,21)	(21,22)	1.913	2.029	0.590	3.69	13.96	
(23,21)	(22,20)	1.086	0.844	0.294	3.42	12.36	
(23,21)	(22,22)	1.160	0.909	0.314	3.47	12.68	
(23,21)	(23,20)	0.792	0.729	0.266	5.37	26.92	Resolved fluorescence
(23,21)	(23,22)	0.695	0.710	0.261	5.42	27.34	
(17,21)	(17,20)	1.152	1.204	0.401	3.65	13.65	
(17,21)	(17,22)	1.124	1.272	0.422	3.63	13.83	
(17,21)	(18,20)	0.894	1.051	0.374	5.15	25.34	
(17,21)	(18,22)	0.842	1.035	0.371	5.19	25.61	
(17,21)	(19,20)	0.746	0.874	0.403	4.70	22.55	

cannot be accurately measured on the pump laser transition, which is contaminated with laser scatter. However, the P/R line intensity ratio is well known from theoretical calculations, so the fluorescence scaling is still accurate.) To carry out this scaling for the resolved spectra obtained in this work, the $5^1\Sigma_g^+(17,21) \rightarrow A^1\Sigma_u^+(18,20)$, $5^1\Sigma_g^+(23,21) \rightarrow A^1\Sigma_u^+(21,22)$, and $6^1\Sigma_g^+(15,19) \rightarrow A^1\Sigma_u^+(15,18)$ transitions were chosen as reference lines, respectively, for the three fluorescence excitation schemes listed above. This scaling method allowed us to expand the total number of measured absolute transition dipole matrix elements.

If the electronic transition dipole moment function $\mu_e(R)$ is known, then it is straightforward to calculate the transition dipole matrix element $\mu = \langle \chi_{vJ} | \mu_e(R) | \chi_{v'J'} \rangle$. However, here we have the opposite situation where the matrix elements are measured, and we want to extract the transition dipole moment function, $\mu_e(R)$, and specifically determine how it depends on R, from these measurements. Each matrix element is an integral over all R values, so a particular matrix element cannot be uniquely attributed to a single R value. However, significant contributions to the matrix element are limited to a range of R where both vibrational wavefunctions are non-zero and have similar phase. This range can be visualized most easily using "accumulation curves,"[21] which are defined as partial

vibrational overlap integrals,

$$ I(R) = \int_0^R \chi_{vJ}(R') \chi_{v'J'}(R')dR'. \quad (3) $$

Examples of these accumulation curves are shown in Figs. 5–7. Specifically, Fig. 5 shows the accumulation curve for a "diagonal" transition, $6^1\Sigma_g^+(v = 19, J = 19) \leftrightarrow A^1\Sigma_u^+(v' = 19, J' = 20)$, where the upper and the lower state vibrational wavefunctions are, for the most part, in phase over their entire overlap range. Thus, we see that, in this case, the integral accumulates approximately uniformly between classical turning points. Figure 6 shows a different type of accumulation curve, represented by the $6^1\Sigma_g^+(v = 15, J = 19) \leftrightarrow A^1\Sigma_u^+(v' = 11, J' = 20)$ transition, in which the integral accumulates for the most part over a fairly narrow range of R values (near the so-called "stationary phase point"). Such a curve implies that the matrix element for that transition is sensitive to the values of $\mu_e(R)$ over a fairly narrow range of R. (We note that the dipole moment function falls significantly between 3 and 4 Å, so the oscillations in the accumulation curve between 3.5 and 4.5 Å, observed in Fig. 6, do not have much effect on the transition dipole matrix element.) Figure 7 shows a third type of accumulation curve, represented by the $6^1\Sigma_g^+(v = 15, J = 19) \leftrightarrow A^1\Sigma_u^+(v' = 16, J' = 20)$ transition,

TABLE II. Transition dipole moment matrix elements (TDMM) obtained from the Autler-Townes splitting measurements and from resolved fluorescence line intensities for various $6^1\Sigma_g^+(v,J) \leftrightarrow A^1\Sigma_u^+(v',J')$ transitions.

$6^1\Sigma_g^+(v,J)$	$A^1\Sigma_u^+(v',J')$	TDMM (Debye) experiment	TDMM (Debye) theory	$|\langle \chi_{vJ} | \chi_{v'J'} \rangle|$	$\overline{R}$ (Å)	$\overline{R^2}$ (Å^2)	
(4,19)	(3,20)	2.284	2.205	0.482	3.42	11.66	
(5,19)	(4,20)	2.158	2.128	0.469	3.43	11.69	
(7,19)	(4,20)	1.000	1.156	0.201	3.16	9.92	
(10,19)	(11,20)	1.596	1.545	0.661	4.14	17.29	Autler-Townes
(13,19)	(14,20)	1.328	1.311	0.531	4.22	18.05	
(15,19)	(15,20)	1.136	1.201	0.359	3.69	13.43	
(19,19)	(19,20)	1.159	1.250	0.444	3.98	15.98	
(22,19)	(21,20)	1.095	1.158	0.323	3.62	12.99	
(15,19)	(9,18)	0.518	0.516	0.086	2.88	8.20	
(15,19)	(9,20)	0.474	0.502	0.084	2.87	8.17	
(15,19)	(10,18)	0.917	0.946	0.161	2.99	8.87	
(15,19)	(10,20)	0.869	0.929	0.158	2.98	8.84	
(15,19)	(11,18)	1.375	1.406	0.249	3.10	9.57	
(15,19)	(11,20)	1.314	1.393	0.246	3.10	9.55	
(15,19)	(12,18)	1.642	1.592	0.301	3.19	10.16	
(15,19)	(12,20)	1.608	1.598	0.301	3.19	10.13	Resolved fluorescence
(15,19)	(13,18)	1.359	1.126	0.258	3.36	11.28	
(15,19)	(13,20)	1.357	1.159	0.263	3.35	11.22	
(15,19)	(15,18)	1.122	1.220	0.366	3.70	13.53	
(15,19)	(16,18)	1.215	0.962	0.369	4.29	18.80	
(15,19)	(16,20)	1.192	1.000	0.386	4.28	18.75	
(15,19)	(17,18)	0.821	0.955	0.617	4.53	20.52	
(15,19)	(17,20)	0.762	0.936	0.614	4.54	20.60	

in which the integral accumulates rapidly over two separate ranges of R, with very little happening in between, and therefore it is difficult to identify the matrix element with a single well-defined range of R.
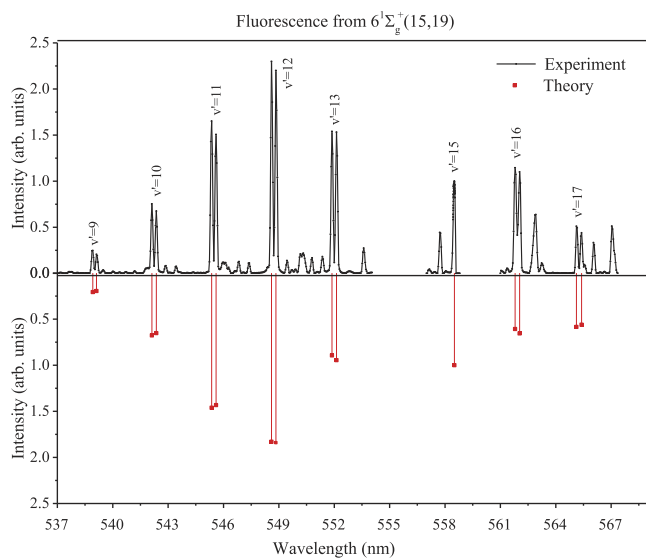
To extract the R dependence of $\mu_e(R)$ from the measured transition dipole matrix elements, one can expand $\mu_e(R)$ in a complete set of functions. A particularly convenient set consists of the powers of R,

$$\mu_e(R) = \sum_{i=0}^{\infty} \mu_i R^i, \tag{4}$$

where μ_i are constants. Then the matrix element can be expressed as

FIG. 4. Resolved fluorescence corresponding to transitions from the Na$_2$ $6^1\Sigma_g^+(15,19)$ level to the $v' = 9, 10, 11, 12, 13, 15, 16,$ and 17 vibrational levels of the $A^1\Sigma_u^+$ state. Several scans were pieced together to create this composite. The $6^1\Sigma_g^+(v = 15, J = 19) \rightarrow A^1\Sigma_u^+(v = 15, J = 20)$ transition was not recorded since the transition frequency corresponds to the laser line where laser scatter saturates the detector. In red are shown the theoretical relative line intensities, calculated using $\mu_e(R)$ from Ref. 6, and the potentials for the $A^1\Sigma_u^+$ and $6^1\Sigma_g^+$ states from Ref. 23 and Refs. 3, 4, and 24, respectively.
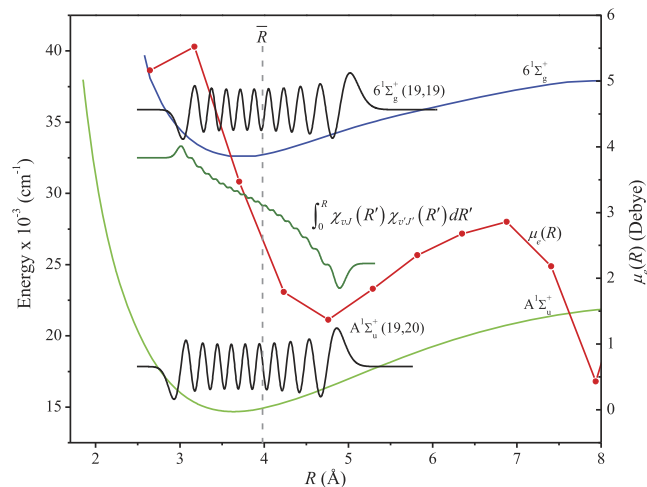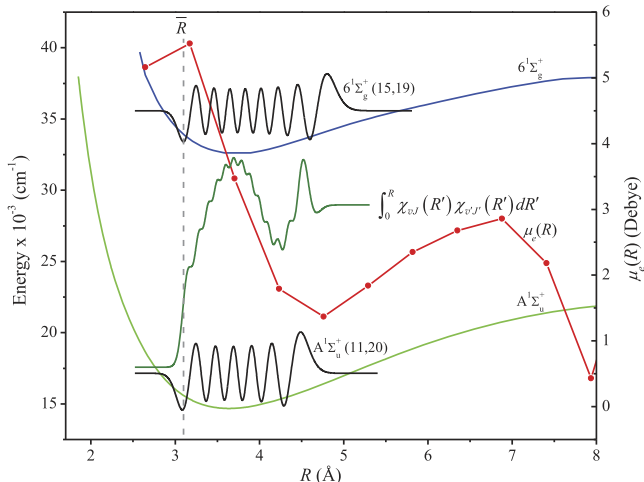

FIG. 5. The accumulation curve for the Na$_2$ $6^1\Sigma_g^+(19,19) \leftrightarrow A^1\Sigma_u^+(19,20)$ transition. The integral (dark green trace) accumulates more or less linearly between 3.0 Å and 5.0 Å. The red line with dots indicates the *ab initio* transition dipole moment function. The dashed vertical line represents the R-centroid value, $\overline{R}$.

FIG. 6. The accumulation curve for the Na$_2$ $6^1\Sigma_g^+$ (15, 19) $\leftrightarrow$ A$^1\Sigma_u^+$ (11, 20) transition. The integral (dark green trace) accumulates most of its value over a narrow range between 3.0 and 3.4 Å (near the so-called "stationary point"). The red line with dots indicates the *ab initio* transition dipole moment function. The dashed vertical line represents the R-centroid value, $\overline{R}$.

$$|\langle \chi_{vJ}| \, \mu_e(R) \, |\chi_{v'J'}\rangle| = |\langle \chi_{vJ}|\chi_{v'J'}\rangle| \sum_{i=0}^{\infty} \mu_i \overline{R^i}, \qquad (5)$$

where

$$\overline{R^i} = \frac{|\langle \chi_{vJ}| \, R^i \, |\chi_{v'J'}\rangle|}{\langle \chi_{vJ}|\chi_{v'J'}\rangle} \qquad (6)$$

is called the ith R-centroid.[22]

In the lowest order approximation to Eq. (5), in which μ_0 = constant, $\mu_{i \neq 0} = 0$ over the range where the integral accumulates, we can write

$$\left|\mu_e\left(\overline{R}\right)\right| = \frac{|\langle \chi_{vJ}| \, \mu_e(R) \, |\chi_{v'J'}\rangle|}{|\langle \chi_{vJ}|\chi_{v'J'}\rangle|}. \qquad (7)$$

This is also a good approximation if the dipole moment function can be accurately represented by a linear function of R over the range where the integral accumulates (see Fig. 5).
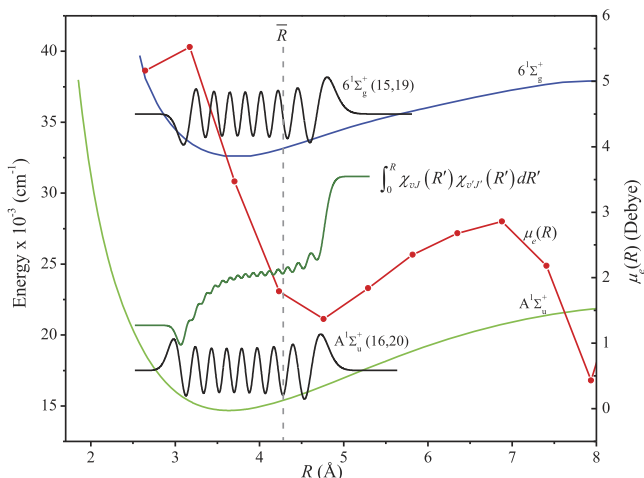

FIG. 7. The accumulation curve for the Na$_2$ $6^1\Sigma_g^+$ (15, 19) $\leftrightarrow$ A$^1\Sigma_u^+$ (16, 20) transition. The integral accumulation (dark green trace) occurs over two separate ranges of R. In this case, it is difficult to identify the matrix element with a single well-defined range of R. The red line with dots indicates the *ab initio* transition dipole moment function. The dashed vertical line represents the R-centroid value, $\overline{R}$.
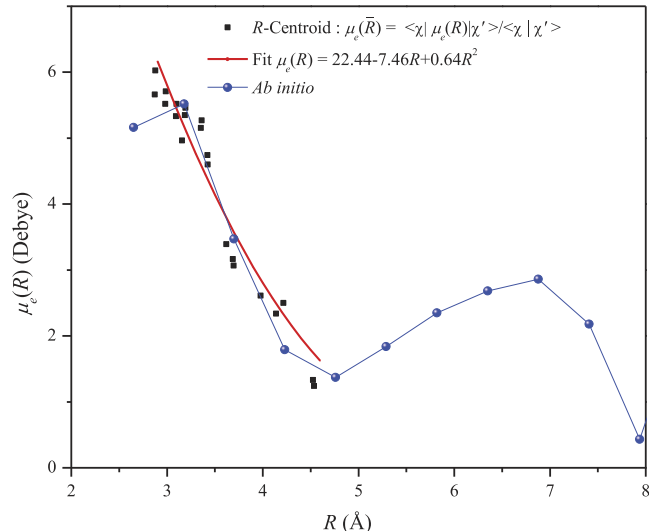

FIG. 8. The electronic transition dipole moment function, $\mu_e(R)$, for the Na$_2$ $6^1\Sigma_g^+ \leftrightarrow$ A$^1\Sigma_u^+$ electronic transition. Solid black squares represent values of transition dipole matrix elements, plotted against R-centroid values. The red curve represents the transition dipole moment function derived from the second order polynomial fit. In the fitting function $\mu_e(R) = 22.4 - 7.46 \, R + 0.64 \, R^2$, $\mu_e(R)$ is given in Debye for R in Å. [Alternatively, the fitting function can be written as $\mu_e(R) = 3.56 - 2.72 \, (R - R_0) + 0.64 \, (R - R_0)^2$ with $\mu_e(R)$ in Debye for R in Å, and $R_0 = 3.70$ Å. See text.] The blue curve is the theoretical result from Ref. 1.

R-centroid values of the $6^1\Sigma_g^+ \leftrightarrow$ A$^1\Sigma_u^+$ electronic transition dipole moment function, $\left|\mu_e\left(\overline{R}\right)\right|$, obtained from the measured transition dipole matrix elements using Eq. (7), are plotted (solid black squares) in Fig. 8. The plot includes all the transitions listed in Table II, except the transitions $6^1\Sigma_g^+$(15, 19) $\leftrightarrow$ A$^1\Sigma_u^+$(16, 18) and $6^1\Sigma_g^+$(15, 19) $\leftrightarrow$ A$^1\Sigma_u^+$(16, 20), for which the R-centroid method is not valid since those accumulation curves exhibit the complicated behavior depicted in Fig. 7.

In the case of the $5^1\Sigma_g^+ \leftrightarrow$ A$^1\Sigma_u^+$ transitions, the accumulation curves for most of the measured transitions are of the type shown in Fig. 7 and only a few transitions with $\overline{R}$ values in the narrow range between 3.6 and 4.0 Å conform to the requirements for validity of the R-centroid approximation. In addition, for a number of transitions, the R-centroid method is inaccurate to such a degree that the calculated $\overline{R}$ value is outside the overlap region of the wavefunctions χ_{vJ} and $\chi_{v'J'}$ (i.e., the region giving non-zero contributions to the accumulation integral). An example of this type of behavior is shown in Fig. 9, where it is clear that plotting the value of the dipole matrix element at the R-centroid value would lead to considerable error in the mapping of the transition dipole moment function $\mu_e(R)$. Thus, we chose not to use the R-centroid method for the $5^1\Sigma_g^+ \leftrightarrow$ A$^1\Sigma_u^+$ electronic transition dipole moment calculations.

When the R-centroid approximation is not valid, it is also possible to model the dipole moment function by a truncated version of the power series expansion given in Eq. (4). Following Refs. 8, 10, and 16, we truncate the power series expansion at the quadratic term $\mu_e(R) = \mu_0 + \mu_1 R + \mu_2 R^2$. The values of the coefficients μ_0, μ_1, and μ_2 are obtained from a multi-parameter fit of Eq. (5) to the set of experimentally measured
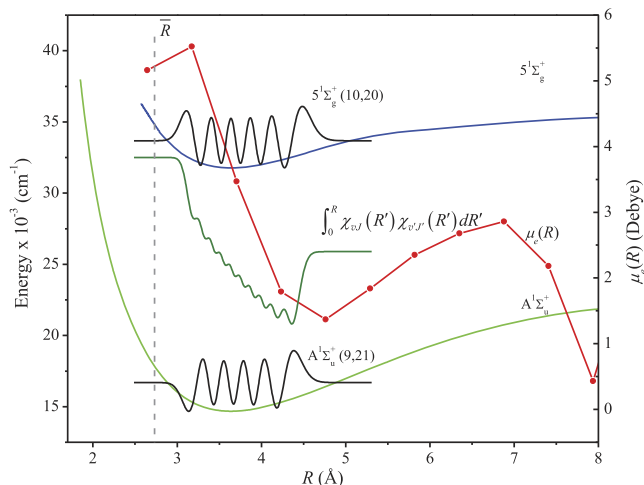
FIG. 9. Example of a transition for which the R-centroid method is inaccurate to such degrees that the calculated $\overline{R}$ value is outside the overlap region of the wavefunctions.

matrix elements $|\langle \chi_{vJ} | \mu_e(R) | \chi_{v'J'} \rangle|$. The ith centroids $\overline{R^i}$ are fixed parameters in the fit, calculated for each transition using potential curves taken from the literature $\{A^1\Sigma_u^+,^{23} 5^1\Sigma_g^+,^2$ and $6^1\Sigma_g^+$ (the inner well from Ref. 3, the potential barrier region from Ref. 24, and the outer well from Ref. 4)$\}$ using the computer program LEVEL 8.0.[25] The results from the second order polynomial fits to the experimental data for the $6^1\Sigma_g^+ \leftrightarrow A^1\Sigma_u^+$ and $5^1\Sigma_g^+ \leftrightarrow A^1\Sigma_u^+$ transitions are also presented in Figs. 8 and 10, respectively.

Alternatively, one can use the mathematically equivalent expression $\mu_e(R) = \mu_0' + \mu_1'(R - R_0) + \mu_2'(R - R_0)^2$, where the dipole moment is expanded about some value R_0, which can be chosen to be the center of the range of R values probed by the experiment. Clearly, the fitting coefficients are related by
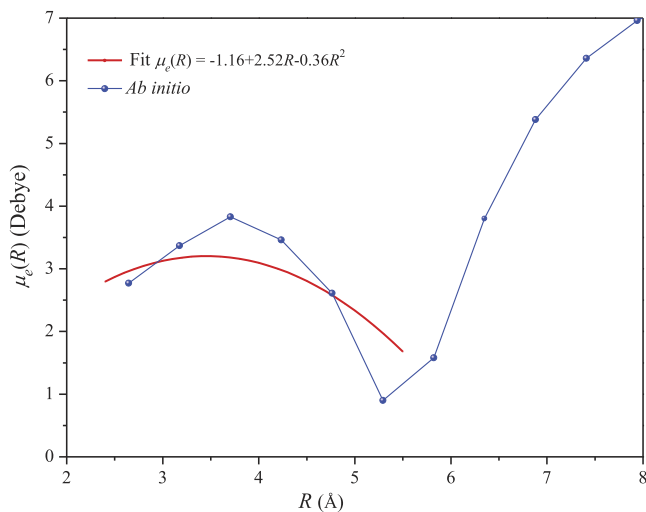

FIG. 10. The electronic transition dipole moment function, $\mu_e(R)$, for the Na$_2$ $5^1\Sigma_g^+ \leftrightarrow A^1\Sigma_u^+$ electronic transition. The red curve represents the transition dipole moment function derived from the second order polynomial fit. In the fitting function $\mu_e(R) = -1.16 + 2.52 R - 0.36 R^2$, $\mu_e(R)$ is given in Debye for R in Å. [Alternatively, the fitting function can be written as $\mu_e(R) = 3.21 - 0.252 (R - R_0) - 0.36 (R - R_0)^2$ with $\mu_e(R)$ in Debye for R in Å, and $R_0 = 3.85$ Å. See text.] The blue curve is the theoretical result for the $5^1\Sigma_g^+ \leftrightarrow A^1\Sigma_u^+$ transition dipole moment function $\mu_e(R)$ from Ref. 1.

$\mu_0' = \mu_0 + \mu_1 R_0 + \mu_2 R_0^2$, $\mu_1' = \mu_1 + 2\mu_2 R_0$, and $\mu_2' = \mu_2$. In this latter case, the fitting coefficients have a more physical interpretation; μ_0' is the average dipole moment at R_0, μ_1' is the average slope of the dipole moment function in the range of R values probed by the experiment, etc.

The linewidth of the coupling transition limits the AT splitting measurements to transitions with relatively large transition dipole matrix elements. Specifically, in our experiment, it was difficult to measure AT splittings for transitions with transition dipole matrix elements smaller than ~1.0 Debye. The signal-to-noise ratio of the resolved fluorescence experiment allowed measurements of transition dipole matrix elements as small as 0.5 D. For $5^1\Sigma_g^+(v, J) \leftrightarrow A^1\Sigma_u^+(v', J')$ transitions, the R range probed in each case, indicated approximately by the $\overline{R}$ values listed in Table I, separate into two groups: one group above ~5.1 Å and the other below ~3.9 Å. The matrix elements corresponding to $\overline{R}$ above 5 Å are all near to or below 1.0 D, while many of the transitions with $\overline{R}$ values between 3.5 and 4.0 Å are typically greater than 2.0 D (see Table I), and hence much easier to observe and optimize with the AT splitting method. We found only a few strong $6^1\Sigma_g^+(v, J) \leftrightarrow A^1\Sigma_u^+(v', J')$ transitions, mainly involving low lying ro-vibrational levels in the $6^1\Sigma_g^+$ state. Thus, the AT measurements were limited in this case to transitions with $\overline{R}$ between 3.16 and 4.22 Å (see Table II). Nevertheless, resolved fluorescence spectra allowed us to expand this range. From the combined AT and resolved fluorescence measurements, we have been able to map the electronic transition dipole moment functions, $\mu_e(R)$, in the range 2.3–5.4 Å for the $5^1\Sigma_g^+ \leftrightarrow A^1\Sigma_u^+$ transition and 2.9–4.5 Å for the $6^1\Sigma_g^+ \leftrightarrow A^1\Sigma_u^+$ transition.

In Figs. 8 and 9, we also show theoretically calculated *ab initio* transition dipole moment functions.[1] As can be seen in the figures, the theoretical dipole moment functions are in very good agreement with the current set of measurements. In Tables I and II, we report experimental and theoretical transition dipole matrix elements. We find that for the $5^1\Sigma_g^+(v, J) \rightarrow A^1\Sigma_u^+(v', J')$ transitions, the percentage difference between the calculated and the experimental transition dipole moment matrix elements is between 2% and 27%, while for the $6^1\Sigma_g^+(v, J) \rightarrow A^1\Sigma_u^+(v', J')$ transitions, the percentage difference is between 0.6% and 23%.

Unfortunately, our measurements were unable to provide a good test of the predicted rapid changes of the transition dipole moment functions, $\mu_e(R)$, with increasing R values beyond 5.5 Å for the $5^1\Sigma_g^+ \leftrightarrow A^1\Sigma_u^+$ transition and beyond 4.5 Å for the $6^1\Sigma_g^+ \leftrightarrow A^1\Sigma_u^+$ transition. These changes in $\mu_e(R)$ are associated with changes in the electronic character of the wavefunction due to interactions with other electronic states. With double resonance excitation schemes, only the inner wells of the $5^1\Sigma_g^+$ and $6^1\Sigma_g^+$ states are accessible from thermally populated levels of the $X^1\Sigma_g^+$ ground state due to weak Franck-Condon Factors (FCFs) associated with excited levels that span larger ranges of R. Thus, our measurements of the $5^1\Sigma_g^+ \leftrightarrow A^1\Sigma_u^+$ and $6^1\Sigma_g^+ \leftrightarrow A^1\Sigma_u^+$ transition dipole moment functions are unable to probe this region of larger internuclear separation. Nevertheless, the theoretically calculated *ab initio* transition dipole moments cover the full range of internuclear distance out to very

large R values. Triple[26] or quadruple resonance[20] experiments could be used for additional experimental mapping of the transition dipole moment internuclear distance dependence if Franck-Condon factors are favorable for these excitation schemes.

IV. CONCLUSIONS

We have combined Autler-Townes splitting measurements of transition dipole matrix elements with OODR resolved fluorescence spectral line intensities to generate experimental transition dipole moment functions, $\mu_e(R)$, for the $5\,^1\Sigma_g^+ \leftrightarrow A\,^1\Sigma_u^+$ and $6\,^1\Sigma_g^+ \leftrightarrow A\,^1\Sigma_u^+$ electronic transitions of Na_2. For strong transitions, we used the Autler-Townes splitting technique[8,10,11,27,28] to obtain *absolute* transition dipole matrix elements. For weaker transitions, we used relative line intensities from resolved fluorescence spectra to obtain *relative* transition dipole matrix elements. These latter were converted to absolute values by scaling against the AT splitting measurements for specific transitions measured by both techniques. From the measured transition dipole matrix elements, we extracted the electronic transition dipole moment function, $\mu_e(R)$, using the R-centroid method and a second order polynomial fit. The experimental results confirm strong variations of these transition dipole moments as a function of internuclear distance. These new experimental measurements allow a stringent test of the recent *ab initio* theoretical calculations reported in Ref. 1. Over the range of internuclear distance accessible by OODR excitation, we find that these theoretical calculations are in good agreement with the experimental transition dipole moment functions, suggesting that the interesting dependence of $\mu_e(R)$ on R, predicted by the theoretical calculations to occur at larger R values, is likely to be reliable.

ACKNOWLEDGMENTS

[1] C. C. Tsai, J. T. Bahns, T. J. Whang, H. Wang, W. C. Stwalley, and A. M. Lyyra, Phys. Rev. Lett. **71**, 1152–1155 (1993).
[2] C. C. Tsai, J. T. Bahns, and W. C. Stwalley, J. Chem. Phys. **100**, 768–774 (1994).
[3] C. C. Tsai, J. T. Bahns, and W. C. Stwalley, J. Mol. Spectrosc. **167**, 429–436 (1994).
[4] T. Laue, P. Pellegrini, O. Dulieu, C. Samuelis, H. Knöckel, F. Masnou-Seeuws, and E. Tiemann, Eur. Phys. J. D **26**, 173–185 (2003).
[5] W. C. Stwalley, J. Mol. Spectrosc. **330**, 14–19 (2016).
[6] A. Sanli, B. Beser, J. R. Edwardson, S. Magnier, E. H. Ahmed, and A. M. Lyyra, J. Chem. Phys. **143**, 104304 (2015).
[7] T. A. Carlson, J. Copley, N. Durić, N. Elander, P. Erman, M. Larsson, and M. Lyyra, Astron. Astrophys. **83**, 238–244 (1980).
[8] S. J. Sweeney, E. H. Ahmed, P. Qi, T. Kirova, A. M. Lyyra, and J. Huennekens, J. Chem. Phys. **129**, 154303 (2008).
[9] A. Lazoudis, E. H. Ahmed, L. Li, T. Kirova, P. Qi, A. Hansson, J. Magnes, and A. M. Lyyra, Phys. Rev. A **78**, 043405 (2008).
[10] E. H. Ahmed, P. Qi, B. Beser, J. Bai, R. W. Field, J. P. Huennekens, and A. M. Lyyra, Phys. Rev. A **77**, 053414 (2008).
[11] J. Qi, F. C. Spano, T. Kirova, A. Lazoudis, J. Magnes, L. Li, L. M. Narducci, R. W. Field, and A. M. Lyyra, Phys. Rev. Lett. **88**, 173003 (2002).
[12] C. R. Vidal and J. Cooper, J. Appl. Phys. **40**, 3370–3374 (1969).
[13] R. Stair, W. E. Schneider, and J. K. Jackson, J. Appl. Opt. **2**, 1151–1154 (1963).
[14] D. R. Skinner and R. E. Whitcher, J. Phys. E: Sci. Instrum. **5**, 237 (1972).
[15] E. H. Ahmed, J. Huennekens, T. Kirova, J. Qi, and A. M. Lyyra, "The Autler-Townes effect in molecules: Observations, theory, and applications," in *Advances in Atomic, Molecular, and Optical Physics*, edited by E. Arimondo, P. R. Berman, and C. C. Lin (Elsevier, Amsterdam, 2012), Vol. 61, pp. 467–514.
[16] O. Salihoglu, P. Qi, E. H. Ahmed, S. Kotochigova, S. Magnier, and A. M. Lyyra, J. Chem. Phys. **129**, 174301 (2008).
[17] E. Ahmed, A. Hansson, P. Qi, T. Kirova, A. Lazoudis, S. Kotochigova, A. M. Lyyra, L. Li, J. Qi, and S. Magnier, J. Chem. Phys. **124**, 084308 (2006).
[18] S. Stenholm, *Foundations of Laser Spectroscopy* (Wiley Interscience, New York, 1984).
[19] T. Kirova, "State selectivity and eigenstate control in molecules using multiple cw lasers," Ph.D. dissertation (Temple University, 2005).
[20] E. H. Ahmed, P. Qi, and A. M. Lyyra, Phys. Rev. A **79**, 062509 (2009).
[21] J. Tellinghuisen, J. Mol. Spectrosc. **103**, 455–465 (1984).
[22] C. Noda and R. N. Zare, J. Mol. Spectrosc. **95**, 254–270 (1982).
[23] P. Qi, J. Bai, E. Ahmed, A. M. Lyyra, S. Kotochigova, A. J. Ross, C. Effantin, P. Zalicki, J. Vigué, G. Chawla, R. W. Field, T.-J. Whang, W. C. Stwalley, H. Knöckel, E. Tiemann, J. Shang, L. Li, and T. Bergeman, J. Chem. Phys. **127**, 044301 (2007).
[24] S. Magnier, P. Millié, O. Dulieu, and F. Masnou-Seeuws, J. Chem. Phys. **98**, 7113–7125 (1993).
[25] R. J. Le Roy, J. Quant. Spectrosc. Radiat. Transfer **186**, 167–178 (2017).
[26] K. Urbanski, S. Antonova, A. Yiannopoulou, A. M. Lyyra, L. Li, and W. C. Stwalley, J. Chem. Phys. **104**, 2813–2817 (1996).
[27] J. Qi, G. Lazarov, X. Wang, L. Li, L. M. Narducci, A. M. Lyyra, and F. C. Spano, Phys. Rev. Lett. **83**, 288–291 (1999).
[28] A. M. Lyyra, H. Wang, T. J. Whang, W. C. Stwalley, and L. Li, Phys. Rev. Lett. **66**, 2724–2727 (1991).